Kinetic energy of eddy-like features from sea surface altimetry

Josué Martínez-Moreno[1], Andrew McC. Hogg[1], Andrew E. Kiss[1], Navid C. Constantinou[1], and Adele K. Morrison[1]

[1]Research School of Earth Science and ARC Center of Excellence for Climate Extremes, Australian National University, Canberra, Australia

Key Points:

- Eddy kinetic energy is decomposed into coherent mesoscale eddies and all other processes (jets, waves and large-scale circulation).
- The coherent eddy component of the eddy kinetic energy in the Southern Ocean has increased during the past two decades.
- The amplitude of the coherent eddy field has increased over the last two decades in the Southern Ocean.

Abstract

The mesoscale eddy field plays a key role in the mixing and transport of physical and biological properties and also in the energy budgets in the ocean. Eddy kinetic energy is commonly defined as the time-varying component of kinetic energy. However, this definition contains all processes that vary in time, including coherent mesoscale eddies, jets, waves, and large-scale motions. The focus of this paper is on the eddy kinetic energy contained in coherent mesoscale eddies. We present a new methodology to decompose eddy kinetic energy into oceanic processes. The proposed methodology uses a new eddy identification algorithm (TrackEddy), based on the premise that the sea level signature of a coherent eddy can be approximated as a Gaussian feature, which then allows for the calculation of kinetic energy of the eddy field through the geostrophic approximation. TrackEddy has been validated using synthetic sea surface height data, and then used to investigate trends of eddy kinetic energy in the Southern Ocean using Satellite Sea Surface Height anomaly (Aviso+). We detect an increasing trend of eddy kinetic energy associated with mesoscale eddies in the Southern Ocean. This trend is correlated with an increase of the coherent eddy amplitude and the strengthening of wind stress over the last two decades.

Plain summary

It is well accepted that climate change results in the intensification of the winds, in particular of those blowing over the Southern Ocean. Despite previous research showing an increase of the high-frequency motions in the Southern Ocean due to the intensification of the winds, we still do not know how swirling vortices of tens to hundreds of kilometers in the ocean have responded to climate change. In this study, we use satellite observations of the sea surface height from 1993 to 2017 to look for changes in the rotating vortices. The focus of our study is on the Southern Ocean as it is one of the areas with more vortices and it plays a key role in controlling the climate system. The developed method extracts the energy of motion of the vortices, and show that this has increased over the past two decades. Using our method, we are able to pinpoint that the energy increase occurs due to an increase in the mean amplitude of the vortices rather than in an increase in number. Finally, the coherent vortices show a clear response to the strengthening of winds in the Southern Ocean.

Corresponding author: Josué Martínez-Moreno, `josue.martinezmoreno@anu.edu.au`

1 Introduction

Ocean variability is composed largely of mesoscale processes, which include coherent eddies, meandering jets and waves. These mesoscale processes are able to mix and transport tracers such as heat, salt and biochemicals across ocean basins, and also to redistribute momentum, potential vorticity and energy (Wyrtki et al., 1976; Chelton et al., 2007; Zhang et al., 2014; Foppert et al., 2017). However, the contribution of each mesoscale process to kinetic energy has not been fully explored, which is crucial to further understand the ocean circulation, ocean biology and to improve global ocean numerical models (Farneti & Delworth, 2010; Beal et al., 2011) .

Kinetic Energy (KE) has been invoked as a measure to understand temporal and spatial oceanic variability (White & Heywood, 1995; Kang & Curchitser, 2017). KE is commonly divided into the Eulerian time-mean or Mean Kinetic Energy (MKE) and the time-varying or Eddy Kinetic Energy (Robinson, 1983). However, to avoid confusion between coherent eddies and time-varying processes, we will use the term Transient Kinetic Energy (TKE) to refer to the time-varying component:

$$\underbrace{\overline{u^2+v^2}}_{\overline{\mathrm{KE}}} + = \underbrace{\bar{u}^2+\bar{v}^2}_{\overline{\mathrm{MKE}}} + \underbrace{\overline{u'^2}+\overline{v'^2}}_{\overline{\mathrm{TKE}}}, \tag{1}$$

where u,v correspond to the horizontal velocity components, $\bar{u}$, $\bar{v}$ the time-mean velocity components and u',v' the time varying velocity components. In many parts of the ocean, transient processes dominate the KE field, i.e., the TKE is more than an order of magnitude greater than the MKE (Gill et al., 1974). These regions include the Alaska Stream, Gulf Stream, Kuroshio Current, East Australian Current, Agulhas Current and the Antarctic Circumpolar Current (ACC) (Wyrtki et al., 1976; Richardson, 1983). These mesoscale-rich regions contain $\sim 70\%$ of the global TKE, and it has been estimated that around 30% of the global TKE arises from coherent eddy processes, as opposed to other transient mesoscale processes (Chelton et al., 2011). This estimate includes the geostrophic velocities within eddy interiors. However, the eddy boundaries do not capture all the Sea Surface Height (SSH) signature attributable only to eddies and may contain signatures from other mesoscale processes.

The temporal evolution of mesoscale-rich regions located in the Southern Ocean (SO) presents an increase in TKE anomaly over the last two decades (Hogg et al., 2015) due to the gradual increase of wind stress over the SO (Marshall G., 2003; Bracegirdle et al., 2013). Some studies suggest that SO is in an "eddy saturated state", i.e., in a state in which the time-mean transport is insensitive to the increase in winds and, therefore, there is readjustment of the transient field to the wind. This hypothesis has been verified several times in numerical models, for example by Hallberg & Gnanadesikan (2001), Meredith & Hogg (2006), Nadeau & Straub (2012) and Marshall D. et al. (2017), but only indications of it have been seen in observations (Böning et al., 2008; Firing et al., 2011; Chidichimo et al., 2014).

It is well known in literature that the surface transient field is highly coupled with the wind forcing. Furthermore, Meredith & Hogg (2006) showed a lag of 2-3 years between the area-averaged TKE and the circumpolar wind stress anomaly. This result was further confirmed regionally using numerical models in the SO (Morrow et al., 2010) and the ACC (Patara et al., 2016). So far, all previous described results include all transient processes in their mean-transient decomposition; thus, the signature of just the coherent mesoscale eddies to the TKE trends remains unclear.

Oceanic coherent eddies have been studied through a wide variety of detection and tracking algorithms, mostly using diagnostic methods or analytical methods. Diagnostic methods build physical intuition to categorize coherent features of the flow based on physical criteria. These methods are mostly based on automated eddy detection algorithms. One of the first studies relied on a measure of rotation and deformation known as the Okubo-Weiss parameter (Chelton et al., 2007). However, the Okubo-Weiss approach has been criticized for its dependence on thresholds and its sensitivity to noise (Chelton et al., 2011; Souza et al., 2011). More recent methods include analysis based on wavelets (Turiel et al., 2007), reversal of the flow field (Nencioli et al., 2010), perturbation of the sea surface temperature (SST) (Dong et al., 2011), the outermost closed Sea Surface Height anomaly (SSHa) contours (Chelton et al., 2011), or a combination of physical and geometric methods (Viikmäe & Torsvik, 2013), single extreme Sea Level Anomaly (SLA) contours (Faghmous et al., 2015), and machine learning using the phase angle between velocity components (Ashkezari et al., 2016). Analytical methods define eddies as coherent structures by mathematical estimations of coherence. Some of these studies include Lagrangian coherent structures identified by material rotation relative to the mean rotation of the deforming fluid volume (Haller et al., 2016; Tarshish et al., 2018), the change in location of a fluid particle induced by infinitesimal changes in its initial position (finite-time Lyapunov exponent) (Beron-Vera et al., 2008; Hadjighasem et al., 2017), and geometrical analysis using transfer operators and invariant manifolds (Froyland et al., 2007; Froyland & Padberg, 2009).

In this study, we present TrackEddy, an eddy tracking and field reconstruction algorithm. The novelty of this algorithm is its capability reconstruct the mesoscale eddy field from global SSHa by fitting optimal anisotropic Gaussians to each identified eddy. Then the reconstructed field can be used to extract the kinetic energy contained in the coherent eddy field. This Python open-source software builds on the algorithms developed by Fernandes (2009), Chelton et al. (2011), Viikmäe & Torsvik (2013), and Faghmous et al. (2015). The new tracking-reconstruction algorithm and kinetic energy decomposition are detailed in Section 2. These methods have been tested using ensembles of synthetic data and the Aviso+ satellite reanalysis (Section 3). The results (Section 4) include a quantitative validation of the method, an update of the Transient Kinetic Energy trend associated only with eddy-like features in the SO and the response of eddies to the westerly wind intensification. Our goal is to use these results to investigate whether the eddy field has a direct response to the wind intensification.

2 Methods

TrackEddy is an autonomous eddy identification, tracking, and reconstruction algorithm, which assumes eddies can be represented as isolated anisotropic Gaussian anomalies. The main and unique characteristic of the TrackEddy algorithm, which differs from previous algorithms (Chelton et al., 2007; Faghmous et al., 2015; Ashkezari et al., 2016) is its capability to reconstruct an optimal Gaussian anomaly for each identified eddy. This Gaussian anomaly can be used to reconstruct the eddy velocities to calculate the TKE associated with the identified coherent eddies.

TrackEddy follows a similar work-flow to previous methods using SSH. It starts with a single snapshot of SSHa, where potential eddies are isolated using study-specific criteria. Generally, an expert describes a strict definition of what will be considered an eddy, by constraining their size and/or shape. This process is then repeated for each levels in which the algorithm identified eddies and all time-step for which the data is available. The following subsections present the TrackEddy algorithm structure, criteria, user-specified values and energy calculation.

2.1 Eddy Identification

TrackEddy starts at the extremum contour of the SSHa field, which corresponds to the maximum value or minimum value of the field anomaly. Then, closed contours are identified and extracted for each contour level defined by the user. The finer the discrete step between contours, the more accurate the eddy sizes and the better the optimal Gaussian fit will be. To be identified as a potential eddy, each closed contour must satisfy three main criteria. First, as Fernandes (2009) proposed, eddies can be identified by using the optimal fitted ellipse. In the case of TrackEddy, the Pearson correlation coefficient of an optimal fitted ellipse should be greater than R_ϵ, where the default value of R_ϵ is 0.9. Second, the eccentricity defined as $e = \sqrt{1 - b^2/a^2}$, where a corresponds to the major axis and b to the minor axis of the ellipse should be greater than a threshold value e_c, which we defined as 0.85. This corresponds to a ratio of a/b about ~ 2. Third, the area of each potential eddy contour should be smaller than $4\pi^2 L_D^2$ (Klocker & Abernathey, 2014), where L_D is the first-baroclinic Rossby radius of deformation (Chelton et al., 1998). If these three criteria are met, the optimal Gaussian is fitted. In order to constrain this optimization, the Gaussian amplitude and location are fixed to the maximum SSHa value inside the closed contour and the coordinates of this maximum, respectively. The Gaussian spread and orientation are then optimized to obtain the best anisotropic representation of the eddy signature. To ensure the best representation of the eddy field, each fitted Gaussian is tested by comparing the absolute difference between the integrals of the original field and the optimal fitted field. If the absolute difference between the fields is larger than 10 percent of its original value the closed contour is discarded. Finally, this process is repeated for each SSHa discrete level and for each time-level of the dataset.

These criteria mostly identify eddies with a single extreme value in each closed contour, but it is possible to identify multiple extrema in different contour levels when eddies merge and/or interact with other features. There are additional sanity criteria which only remove eddy candidates if the SSHa profile over the minor and major axis of the fitted ellipse do not approximate a Gaussian, or if features are mostly surrounded by land. For the eddy identifications from the SSH fields in this study we verified that these additional criteria discarded less than 1% of the identified eddies, however they are crucial to avoid unrealistic Gaussian fits. For more details on the TrackEddy algorithm, the reader is referred to the online documentation at `https://trackeddy.readthedocs.io`.

Default user-specified values for $R_\epsilon = 0.9$, $e_c = 0.85$ and an SSHa level interval of $1cm$ were optimized to obtain the best qualitative eddy reconstruction from the AVISO+ satellite dataset and these values are used in the applications of TrackEddy to the synthetic and satellite data presented in Section 4.

2.2 Kinetic energy decomposition

Kinetic Energy is commonly separated into the mean and transient components by a Reynolds decomposition. At a given time, the velocities (u, v) are split into their time-mean $(\bar{u}, \bar{v})$ and time-varying components $(u' = u - \bar{u}, \quad v' = v - \bar{v})$. We further spatially decompose the time-varying velocities (u', v') into, e.g.,

$$u' = u'_e + u'_r, \tag{2}$$

and similarly for v'. Where u'_e is the eddy velocity and u'_r the residual velocity. The eddy velocity (u'_e) corresponds to the geostrophic velocities inside each coherent eddy-like feature identified by the TrackEddy algorithm and the residual (u'_r) is the difference between the transient velocities and the eddy velocity. Based on this velocity decomposition, TKE can be written as:

$$\underbrace{{u'}^2 + {v'}^2}_{\text{TKE}} = \underbrace{{u'}_e^2 + {v'}_e^2}_{\text{TEKE}} + \underbrace{{u'}_r^2 + {v'}_r^2}_{\text{TRKE}} + \underbrace{2({u'}_e{u'}_r + {v'}_e{v'}_r)}_{\text{TRKE}_c}, \tag{3}$$

where the TEKE term contains only energy from eddy processes, TRKE contains energy from all the non-eddy processes, and TRKE_c are cross terms or the overlap between the eddy field and the residual.

3 Algorithm validation

We evaluate the quality of identified features by testing the code with four ensembles of synthetic fields, each with 1000 members, created by the addition of randomly distributed Gaussian features. Each member contained a random number of Gaussian perturbations ($5 < n < 20$) at random locations with normal-distributed random properties. Each Gaussian has a polarity of -1 or 1, an orientation from 0 to 360°, and an amplitude and major axis between 0.7 and 1.3. The first and simplest experiment is a set of randomly distributed Gaussians constrained to not overlap with any other Gaussian feature within a circle with radius of their major axis (no interaction control). Figure 1a is an example of a single member with 17 Gaussian features of varying size. Figure 1b shows the reconstruction of the features verifying that they have the correct location and the right Gaussian spread and orientation. The domain integrated KE of the non-interacting control and the reconstruction is shown in figure 1c. Therefore, TrackEddy can estimate the energy contained by non-interacting isolated Gaussians, that represent non-interacting eddies.

Non-interacting eddies are a simple idealization of the ocean eddy field. We now consider progressively less idealized cases, beginning with interacting Gaussian features (interacting control). The second ensemble allows overlapping between Gaussians, which produces complex structures, such as the generation of elongated features when two or more Gaussians partially overlap, or large slopes when Gaussians of different polarity overlap. Figures 1d & e show a sample member and its reconstruction from the interacting control ensemble. When Gaussians with opposite polarities partially overlap, the algorithm is able to identify and reconstruct the features. In the case of Gaussians with the same polarity, if each feature has an identifiable maximum, then the algorithm will fit the corresponding number of Gaussians shown in figures 1d & e. However, almost complete overlaps with identifiable independent closed contours, containing minimal information to optimize a Gaussian fit, will be represented poorly (figure 1e). The integrated KE of the interacting control against the reconstruction shows a good estimation and the standard deviation for the 1000 ensemble members is 5.38, which is larger than the standard deviation of non-interacting experiment (2.90). We do not expect every feature to be perfectly reconstructed, particularly when the eddy-like features overlap. However, TrackEddy is able to identify and reconstruct the majority of features, and thereby represent the eddy signature and their kinetic energy content.

To attempt more "realistic" evaluations, the remaining experiments use the same field as the interaction control experiment, but with background perturbations like planetary waves (figure 1g) and jets (figure 1j). The experiment with planetary-like waves is analogous to the interacting control, where most eddies are identified except when the Gaussians overlap almost completely. Strongly interacting Gaussians are still poorly represented (figure 1h). Note that the amplitude of the reconstructed Gaussians depends on whether the background anomaly has the same or opposite sign. Thus, a larger spread of the standard deviation ($\sigma = 7.99$) is generated when comparing the reconstructed KE and the interacting control energy. Furthermore, when the jet-like background field (in which the sinusoidal pattern has a length-scale similar to the Gaussian) is used, most of the features are identified. However, there are some false positive identifications as shown in figure 1k and an even larger standard deviation ($\sigma = 8.84$). Despite the misreadings in amplitude and number of features for both background perturbations, figures 1i & l show the reconstruction of KE using the TrackEddy algorithm approximates the energy contained by the control experiments.

In each of the evaluation tests shown here, the overall reconstruction of KE using the TrackEddy algorithm approximates the energy contained by the control experiments. Therefore, we conclude that our algorithm is capable of representing and extracting the energy, even when there is a background perturbation field. In the next

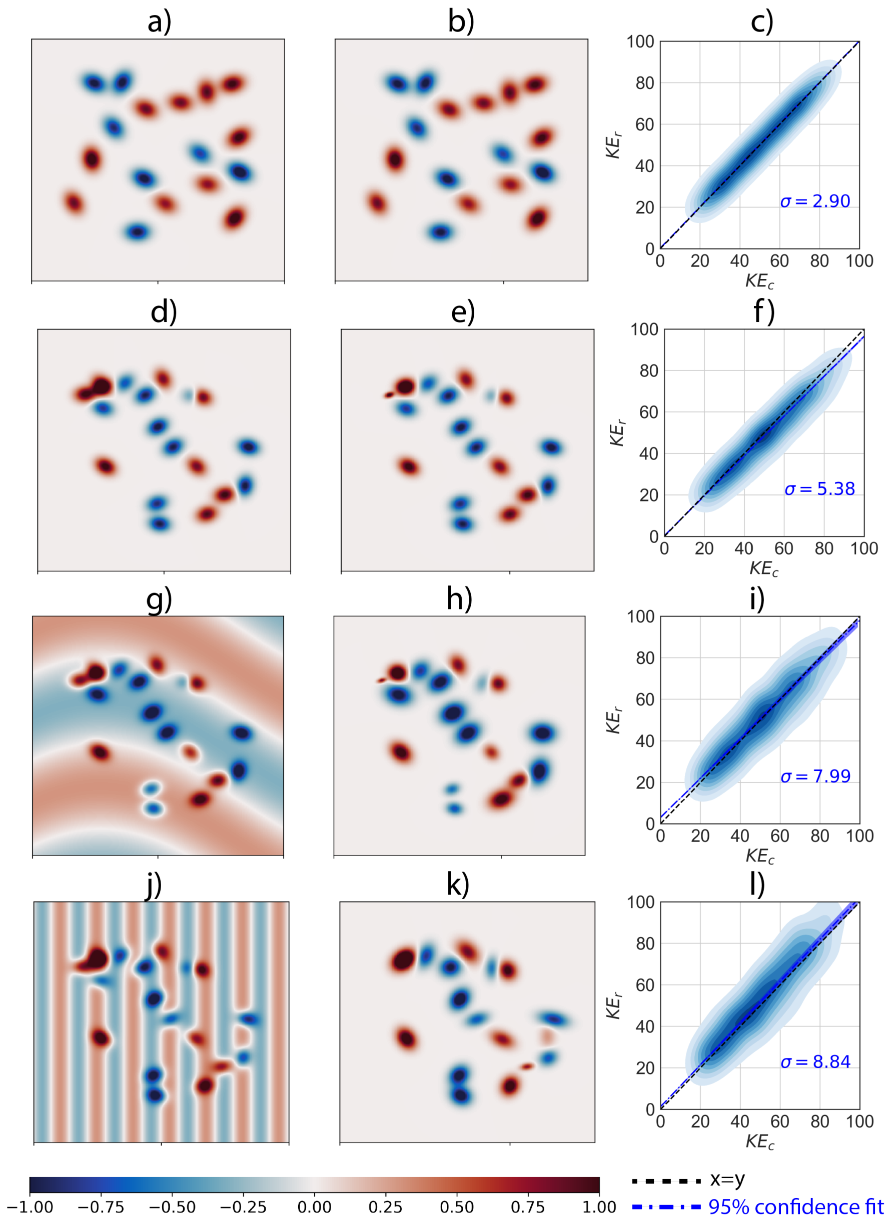

Figure 1. Field plots show a single member of each synthesized SSH dataset ensembles and its reconstruction by TrackEddy algorithm ; (a-b) no interaction control, (d-e) interaction control, (g-j) interacting eddies and propagating waves and (j-i) interacting eddies and jets. Additionally, the 1000 members density distribution of the integrated control field KE (KE_c) versus the integrated reconstructed field kinetic energy (KE_r) correspond to panels c, f, i, and l.

section, we proceed to use TrackEddy to reconstruct the eddy field and energy from the satellite SSHa field.

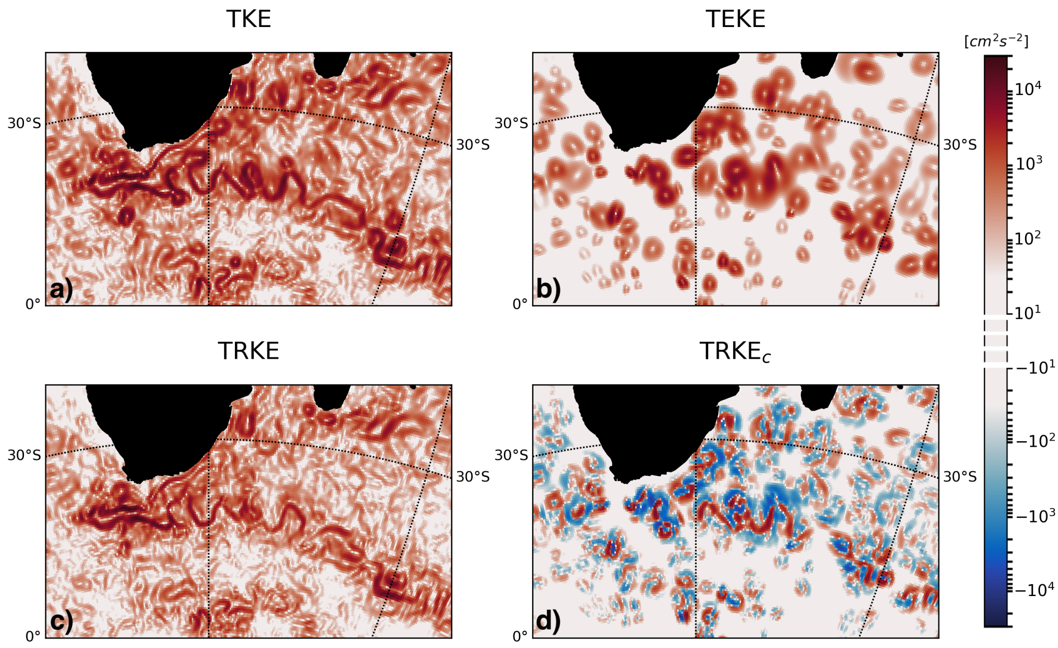

Figure 2. Magnitude of Transient Kinetic Energy and its decomposition in the Agulhas Current for a snapshot on January 1st 2016. a) Transient Kinetic Energy, b) Transient Eddy Kinetic Energy or the energy of eddy processes, c) the Transient Residual Kinetic Energy or energy of jets and waves, and d) the cross terms which correspond to the overlap between processes.

4 Results

After diagnosing the capabilities of TrackEddy, we implemented the algorithm on the global gridded AVISO+ satellite Sea Surface Height (SSH) product derived from all the available satellites from CMEMS (E.U. Copernicus Marine Service Information). The analyzed period covers from January 1993 to December 2017 on a $0.25° \times 0.25°$ longitude/latitude grid. Sea Surface Height anomaly (SSHa) data was obtained by removing the historical SSH climatology from 1993 to 2012 for each individual SSH snapshot and also removing the moving average of a 20° latitude/longitude kernel to preserve only mesoscale features. The eddies identified using TrackEddy from the satellite AVISO+ dataset are publicly available (http://dx.doi.org/10.25914/5cb6859e4df3e).

4.1 Transient Kinetic Energy

Figure 2 shows a snapshot from January 1st 2016 of the TKE, TEKE, TRKE and TRKE$_c$ fields in the Agulhas Current region. Figure 2a shows a TKE snapshot where ring-like features and filaments can be observed, corresponding to coherent eddies, and jets respectively. The signature of coherent eddies in Kinetic Energy or TEKE in the Agulhas region is shown in figure 2b. This snapshot shows elliptical areas with large KE values. Each individual eddy is shown as a ring with two local maxima on either side of the major axis (figure 2b). These local maxima result from the elliptical nature of the reconstructed eddies, but also it has been observed and attributed to dipole pattern for the downwind momentum transport mechanism over the eddy features (Chelton et al., 2004; Frenger et al., 2013).

The Southern Ocean time-mean values of TKE and TEKE are shown in figure 3a&b respectively. The mean TKE (figure 3a) is several orders of magnitude larger at the western boundary currents and the ACC than any other region in the SO. The mean TEKE (figure 3b) also shows the pathways of the ACC and the western boundary currents, which are key in the generation of coherent eddies. Finally, TEKE is fundamental to the understanding of the TKE as on average it explains 37% of TKE in the Southern Ocean with a temporal variability of 10%, similar to the global estimate proposed by Chelton et al. (2011).

The TRKE snapshot (figure 2c) shows filaments which mostly correspond to jets, while some ring-like features are still observable, corresponding to misidentified eddies by our algorithm. Again, the largest signatures in figure 3c are located in the ACC and western boundary currents. The mean TRKE (figure 3c) now mostly consists of jets, meanders and waves and these processes contain approximately $65 \pm 10\%$ of the TKE in the Southern Ocean. Finally, the absolute magnitude of the cross terms ($|\mathrm{TRKE}_c|$) is shown in figure 3d. $|\mathrm{TRKE}_c|$ corresponds to the mismatches and overlaps between the reconstructed coherent eddy velocities and the geostrophic velocities from SSHa due to kurtosis and misrepresentation of the fitted Gaussians. The absolute magnitude of this field is similar to TEKE, however, the structure mostly contains a "random" spatial distribution of positive and negative values (figure 2d). Therefore, $\overline{\mathrm{TRKE}_c}$ is much smaller than any of the other components (figure 3), where the average signature of TRKE_c over TKE is $1.0 \pm 0.5\%$, so TRKE_c will be neglected as it is one order of magnitude smaller than the other components.

The proposed decomposition is a robust method to separate coherent eddies from the transient field. A key result is the dominance of the $\overline{TEKE}$ in localized areas in the SO shown in figure 4a, in which white contours show regions with $\overline{TEKE} \geq 183 cm^2/s^2$ (2σ), more than 3 times the SO average of $\sim 48\ cm^2/s^2$. The contours show eight main hotspots in the Southern Ocean. Four of these regions are associated with interactions between the ACC and major bathymetric features and the rest correspond to western boundary currents. The prominent topographic features are the Drake Passage (DP; 155°W - 130°W), Pacific Antarctic Rise (PAR; 75°W - 45°W), Southwest Indian Ridge (SWIR; 20°E - 40°E), Kerguelen Plateau (KP; 81°E - 96°E), Southeast Indian Ridge (SEIR; 115°E - 160°E), Macquarie Ridge (MR; 160°E - 180°E). The western boundary currents correspond to the Agulhas Return Current (ARC; 10°E - 83°E), the Brazil-Malvinas Confluence (BMC; 60°W - 25°W). These hotspots in TEKE have strong eddy activity, and they have been shown to play a key role in the SO exchange of heat and carbon and upwelling pathways (Woloszyn et al., 2011; Dufour et al., 2015; Foppert et al., 2017; Tamsitt et al., 2017).

The TEKE hotspots also have a co-located large signature in the mean amplitude of the reconstructed coherent eddy field ($\overline{E_{amp}}$) for the satellite period (figure 4b), which highlights regions that are dominated by eddies of one polarity. For example, all western boundary currents have a large negative value of $\overline{E_{amp}}$ north and positive $\overline{E_{amp}}$ signature south of the climatologic western boundary currents. This signal is a consequence of the meanders becoming unstable and generating cold core eddies on one side of the climatologic jet location and warm cores eddies on the other side. Meanwhile, in the Pacific and Atlantic basins there is a positive eddy amplitude signature north of the ACC (dashed lines), while the Indian sector has a negative signature. Figure 4c further shows the $\overline{TEKE}$ (green curve) and $\overline{E_{amp}}$ (blue curve) meridionally integrated across the climatological ACC ($\overline{SSH} = -0.8$ to 0.2 m), as well as the major topographic features denoted by horizontal lines. Note that downstream of each of the major topographic features with a TEKE peak there is a change in the polarity of $\overline{E_{amp}}$. In the case of Pacific Antarctic Rise, Brazil-Malvinas Confluence, Agulhas Return Current, Southwest Indian Ridge, and Southeast Indian Ridge there is a transition from positive to negative $\overline{E_{amp}}$, while at Kerguelen Plateau and Macquarie Ridge

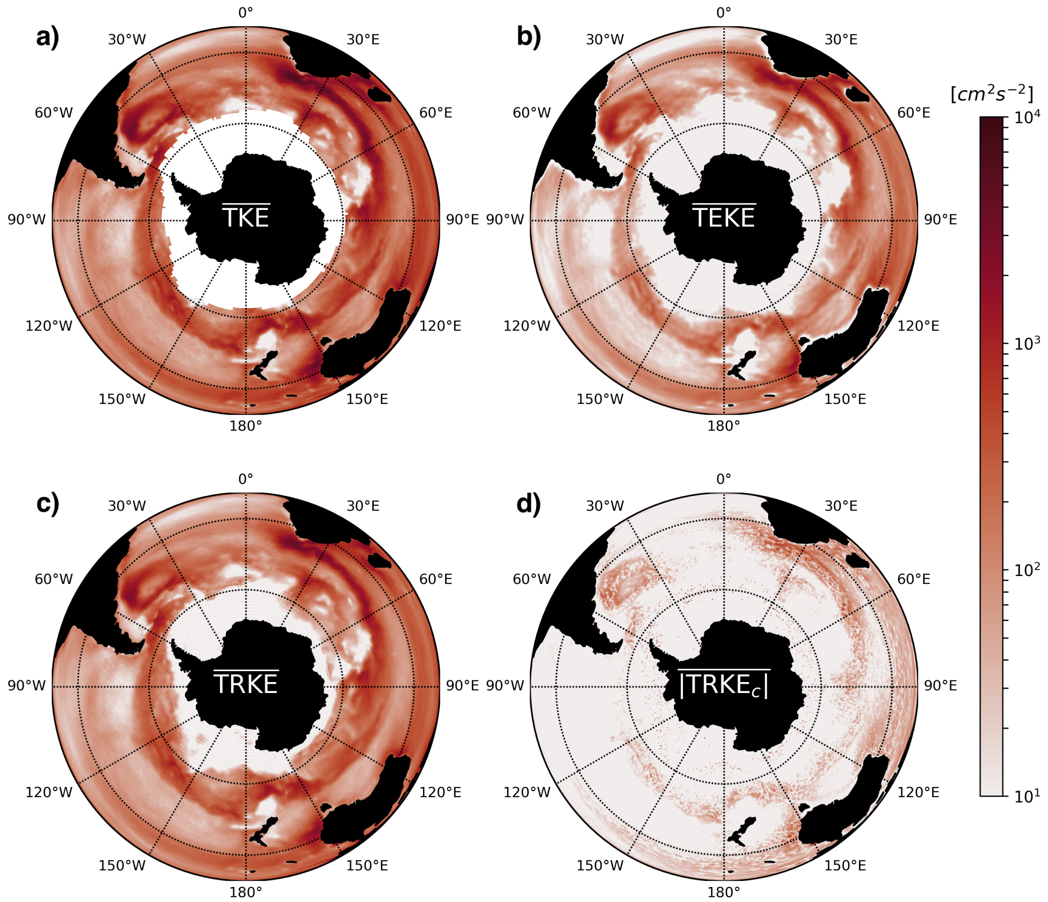

Figure 3. Magnitude of average Transient Kinetic Energy and its decomposition in the Southern Ocean reconstructed from satellite SSHa from 1993 to 2017. a) Transient Kinetic Energy, b) Transient Eddy Kinetic Energy or the energy of eddy processes, c) the Transient Residual Kinetic Energy or energy of jets and waves, and d) the cross terms which correspond to the overlap between processes.

the transition is from negative to positive $\overline{E_{amp}}$. We suspect this transition between polarities to the characteristic signature south of the western boundary currents, which in some areas is included within the ACC contour. However, this change in polarity is not always located south of the western boundary currents and therefore it should be further investigated.

4.2 Trends

Now we further explore the reported increase of TKE trends over the satellite record (Hogg et al., 2015). Figure 5 shows time series of the running annual average anomaly of TKE, and its decomposition (TEKE and TRKE) spatially averaged over the SO and three sectors in the SO similar to those used by Meredith & Hogg (2006) and Hogg et al. (2015): SO: 0°E - 360°E, 30°S - 60°S; Indian Ocean: 40°E - 150°E, 44°S - 57°S; Pacific Ocean: 150°E - 288°E, 48°S - 62°S; and Atlantic Ocean: 325°E - 10°E, 46°S - 56°S. These regions are depicted by the orange dashed boxes in figure 4a. Dashed lines show the linear trends with 95% confidence according to the Theil-Sen estimator. Note that the magnitude of the variability remains constant in time for all

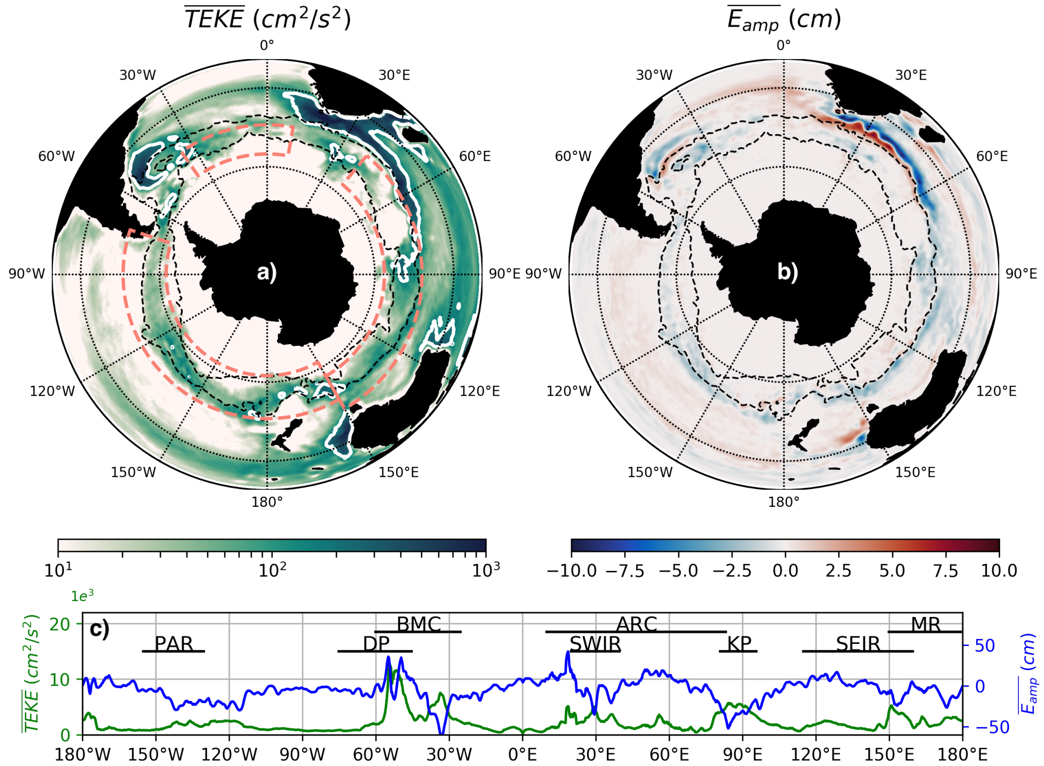

Figure 4. TEKE and mean eddy amplitudes maps of the Southern Ocean with mean circumpolar streamlines defining outer edges of the ACC band ($\overline{SSH} = -0.8$ to 0.2 m). a) $\overline{TEKE}$ climatology over the satellite altimetry era from 1993 to 2017. White contours correspond to values larger than 183 cm^2/s^2. b) $\overline{E_{amp}}$ or mean eddy amplitude shows areas with high eddy intensity and their polarity dominance. c) Meridional sum of $\overline{TEKE}$ and $\overline{E_{amp}}$ by longitude within the ACC band defined by black dashed lines in (a,b). Orange boxes in a) show the ACC Pacific, Indian and Atlantic basins.

basins, and there are no step changes where the number of satellites has increased. Therefore, we infer the increasing signal is an intrinsic response of the coherent eddy field.

The SO energy anomaly magnitude is smaller than the Pacific and Indian sector, as it includes large areas of the South Pacific, South Atlantic and Indian gyres where the KE content is lower than the other sectors which were selected to mostly cover sections of the ACC. However, significant increasing trends are observed for each KE component (figure 5a & table 1). During most of the record the variability of TKE is followed closely by TEKE and TRKE. However, we would like to highlight the period between 2013-2016, where the TEKE shows a different response, which indicate changes in the eddy properties. However, it's necessary to explore it in more detail.

The Pacific sector of the SO shows significant increasing trends for the transient kinetic energy and all its components. The TKE trend in the Pacific is made up of $26 \pm 11\%$ of the TEKE trend and $76 \pm 11\%$ of the TRKE trend. The Indian sector also shows an increasing trend for TKE, TEKE and TRKE. The contribution of TEKE to the TKE trend is $30 \pm 17\%$, while TRKE is responsible of $72 \pm 11\%$ of the TKE trend. The content of TEKE is larger in the Indian than the Pacific sector, as the Indian

Table 1. Detected trends of TKE by Hogg et al. (2015) from satellite tracks, AVISO+ gridded data and decomposition trends (TEKE, TRKE) over each basin in cm^2/s^2 per decade.

	SO	Pacific	Indian	Atlantic
TKE (Hogg et al. 2015)	—	14.9 ± 4.1	18.3 ± 5.1	4.0 ± 3.7
TKE	14.0 ± 1.8	18.2 ± 3.0	22.3 ± 4.1	3.3 ± 2.7
TEKE	3.8 ± 0.7	5.8 ± 1.2	5.4 ± 1.7	0.3 ± 1.3
TRKE	9.4 ± 1.4	12.0 ± 2.2	14.7 ± 3.0	3.0 ± 1.9

region contains a portion of the Agulhas return current. Meanwhile, the Atlantic sector only shows a significant increase in TKE and TRKE, but TEKE trend is within the error.

The detected TKE trends found from gridded data using TrackEddy and the geometrical reconstruction of the eddy field are consistent with the trends calculated from satellite tracks by Hogg et al. (2015) (Table 1). According to Hogg et al. (2015), the TKE trends found in gridded data could be underestimated due to the interpolation from satellite tracks to gridded by a factor of 1.9 in the Pacific, 1.7 in the Indian and 1.6 in the Atlantic. Therefore, the detected trends could be larger than reported.

The increase in the TKE signal is composed mostly of the addition of the TEKE and TRKE trends. Even when TEKE fluctuates between 20 to 50 percent of the TKE signature, it can be attributed uniquely to coherent eddies, while the residual TRKE still includes large scale jets, meanders, wave processes and some misidentified eddies. This decomposition has identified the contribution of mesoscale processes to the observed trend in the SO transient kinetic energy; the adjustment of properties of the coherent eddy field are explored in the following Section 4.4.

4.3 Eddy Characteristics

The increase in TEKE previously described highlights that part of the observed Southern Ocean TKE trend is due to changes in the coherent eddy field. These results suggest that one or more eddy properties (number, amplitude, area, and/or eccentricity) have increased over the last two decades. We investigated the eddy characteristics responsible for the positive TKE trends using the individual geometric characteristics of each identified eddy from TrackEddy output. After diagnosing the time series of each of the properties, the variables showing a robust trend were the number of eddies (E_n), the absolute eddy amplitude ($|E_a|$), defined as the maximum absolute amplitude within each identified eddy, and the eddy area (E_{area}), defined as the box containing the identified close contour.

The average detected number of eddies in the SO over the satellite record is around 920 per daily snapshot. Figure 6a shows daily variability, which presents a seasonal cycle, potentially attributed to the seasonality of the mixed layer (Nardelli et al., 2017). Additionally, the running annual mean shows a significant decrease of -15.17 eddies per decade. This signal is counter-intuitive, as it shows that increase in TEKE does not depend on the number of identified coherent mesoscale eddies. We still do not know the mechanisms which drives the decrease in the number of eddies, but we believe that it could be crucial to further understand eddy saturation.

Meanwhile, the mean eddy amplitude and mean eddy area have increased at a rate of 0.41 cm and 129.23 km^2 per decade respectively (figures 6b,c). Therefore,

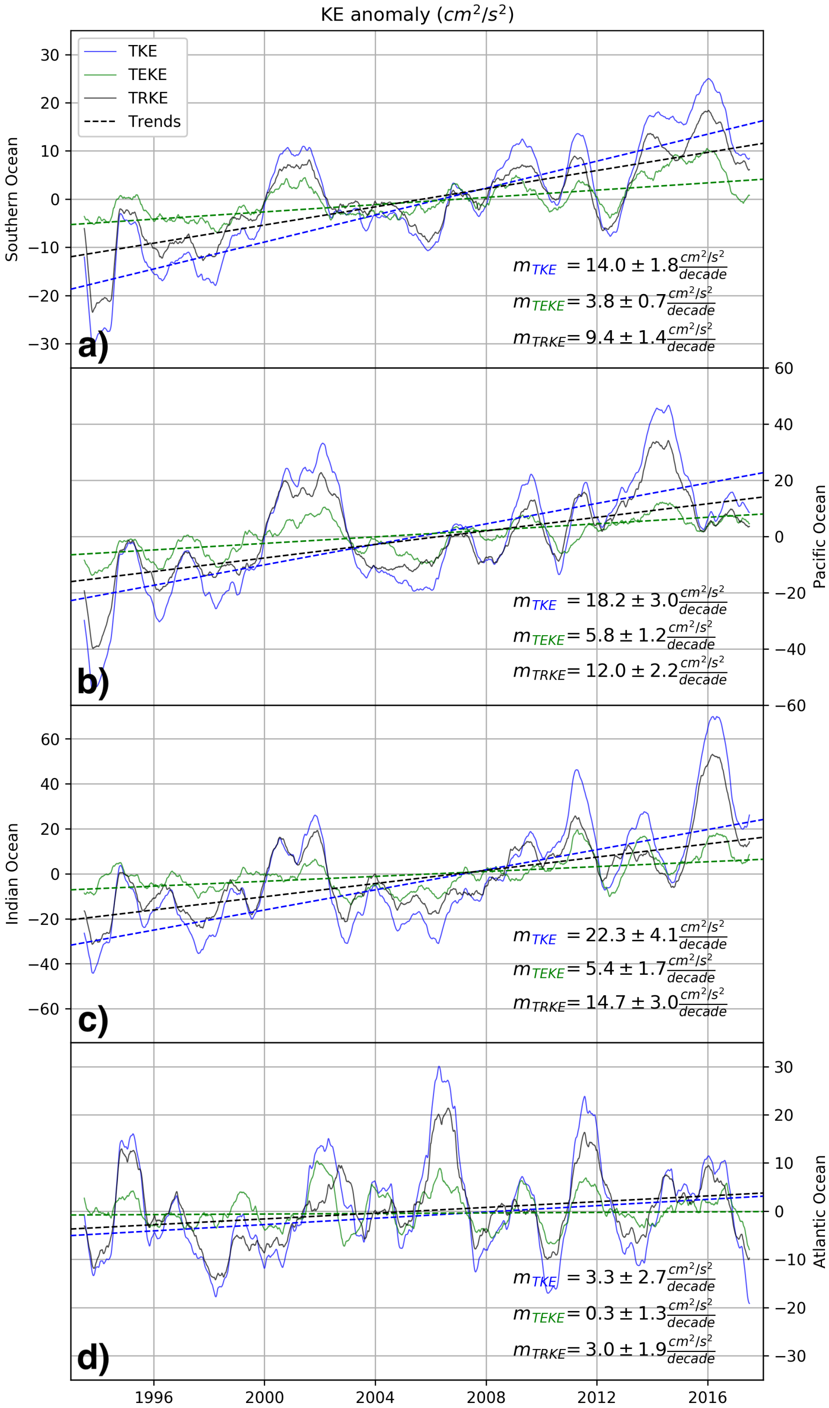

Figure 5. Time series of transient kinetic energy (blue line), transient eddy kinetic energy (green line) and transient residual kinetic energy (black line) time anomalies from satellite data for the a) Southern Ocean (SO) and three SO sectors: b) Pacific Ocean , c) Indian Ocean and d) Atlantic Ocean. Solid lines show running annual means, while the dashed line shows the 95% confidence satellite altimetry era trend.

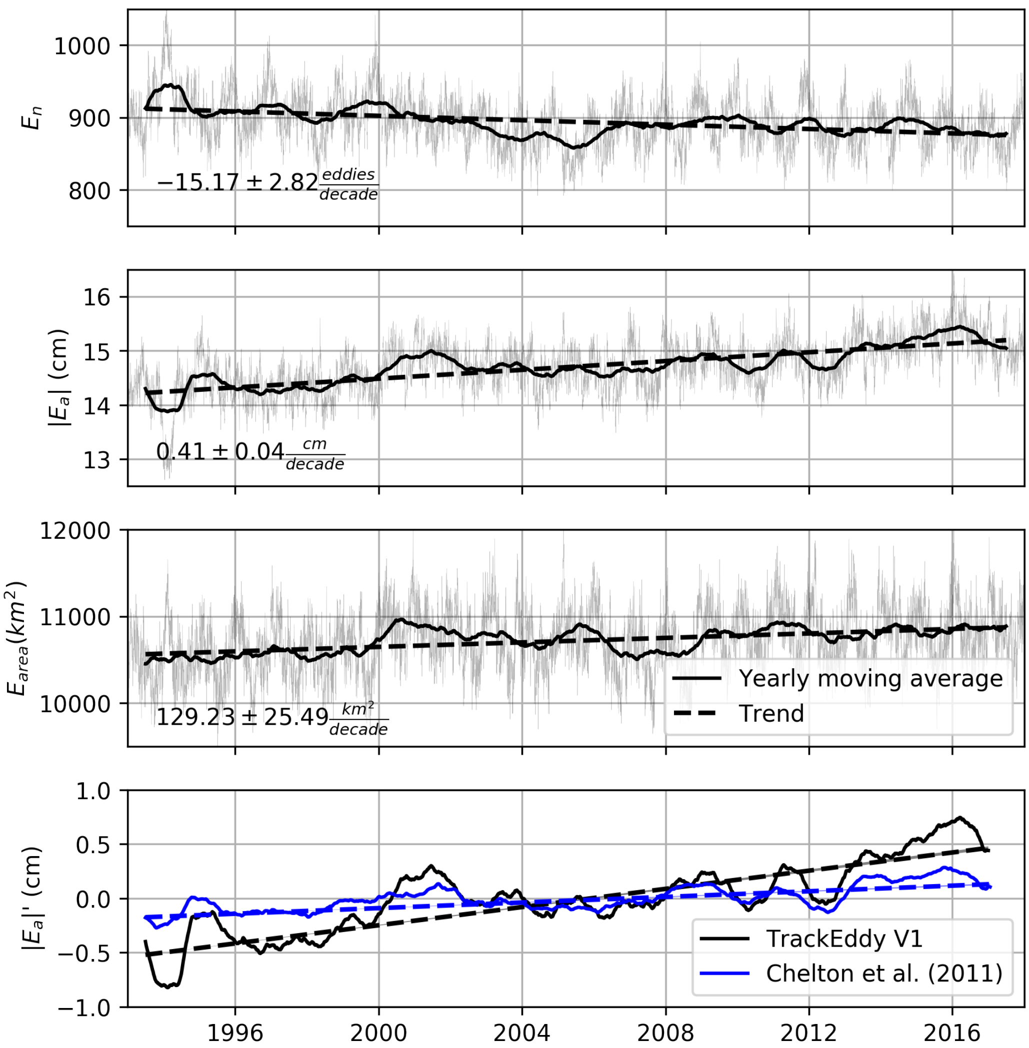

Figure 6. Time series of a) the number of detected eddies, b) the eddy mean amplitude and c) the eddy mean area over the Southern Ocean from TrackEddy, and d) the comparison between the normalized TrackEddy mean eddy amplitude time anomaly ($|E_a|'$) and Chelton et al. (2007) . Colored lines show running annual means, while the dashed line shows the satellite altimetry era trend.

TEKE trends are mostly due to the intensification of the eddy amplitude with a small increase in the eddy area. The eddy amplitude intensification qualitatively agrees with the trends computed from Chelton et al. (2007) (figure 6d). Note that the mean eddy amplitude variance as computed by TrackEddy is around 10 times larger than results from Chelton et al. (2007), and the detected trend by TrackEddy ($0.43 cm/decade$) is three times larger than Chelton's ($0.13 cm/decade$). This difference is attributed to how both algorithms report the amplitude of eddies. The TrackEddy definition corresponds to the maximum SSHa within the eddy, while Chelton's algorithm uses the maximum SSHa value minus the contour level where the eddy was identified, which filters the detected signal.

As discussed in the introduction previously, the transient field has responded to the intensification of the westerly winds in the SO (Marshall G., 2003; Bracegirdle et al., 2013). Furthermore, previous studies have shown a lagged response between the wind stress and TKE trends Hogg & Blundell (2006); Morrow et al. (2010); Patara et al. (2016). Here, we further explore the relation between the de-trended and normalized mean eddy amplitude and the de-trended and normalized wind stress calculated using the bulk formula without the ocean state component from JRA55-do (Tsujino et al., 2018) (figure 7).

The SO time series of mean eddy amplitude has a weak correlation with the SO wind stress (figure 7a). The lagged cross-correlation of these time series has two predominant local maxima approximately at 1 and 3 years (figure 7b). Hogg & Blundell (2006) suggested that the slow response corresponds to strong topographic steering due to the vertical momentum transport from interfacial form stress of the transient field, while a possible hypothesis to the fast response could be the direct enhancement-readjustment of baroclinic instabilities. The Pacific Ocean cross correlation has a clear maximum lag at 3 years (figure 7c-d). Therefore, the response of the eddy field in the Pacific sector is mostly dominated by the topographic steering mechanism. The Indian Ocean has two local maxima in the cross correlation (figure 7e-f), where the largest peak has a lag of 8 months, again suggesting a fast response of the eddy fields to the winds. Finally, the lagged cross-correlation in the Atlantic Ocean is not significant, however it still show three maxima at 1, 3 and 5 years (figure 7g-h).

The SO eddy field could be responding the winds through a fast-baroclinic adjustment and a slow interfacial transfer of momentum. Moreover, this response varies in each of the basins, which suggests a spatial dependence possibly related to the main topographic features of the SO basins.

5 Discussion and Conclusions

We propose a new eddy-reconstruction algorithm to extract the kinetic energy contained in mesoscale coherent eddies. Our synthetic tests show that the Transient Eddy Kinetic Energy is well estimated by TrackEddy and the method is sensitive enough to extract the energy signature contained only by coherent eddies. Taking advantage of the 23 years of the AVISO SSH, we identified and reconstructed each eddy based on its geometric parameters: amplitude, area, and orientation.

The Transient Eddy Kinetic Energy (TEKE), that is the transient energy contained in coherent eddies, in the Indian and Pacific sectors of the SO exhibits a significant trend over the satellite altimetry era. Consistent with previous studies (Hogg et al., 2015), Transient Kinetic Energy (TKE) trends are explained by a combination of the changes in the eddy and residual fields, where TEKE explains 1/3 of the TKE while TRKE explains the rest 2/3. Note that this is still an underestimation of the eddy contribution as TrackEddy does not capture all eddies due to its more rigorous criteria. However, its clear that the contribution of non-eddy transient processes (TRKE) are crucial to further understand the transient kinetic energy.

In addition, we find an intriguing decadal increase in the eddy amplitude in the SO since 1993, which is responsible for the increase in TEKE. There is a correlation between the 1-3 year lagged wind stress and the eddy amplitude on the SO, which could be the response of the eddy field to a fast-baroclinic and a slow interfacial form stress response. The largest cross-correlations were found in the Pacific and Indian sectors and they are consistent with the lagged TKE response of 2 to 3 years to the intensification of the SO westerly winds. Overall, these results suggests a response of the coherent eddy field to intensification of westerly winds in the SO, and this is consistent with the lag found in previous studies.

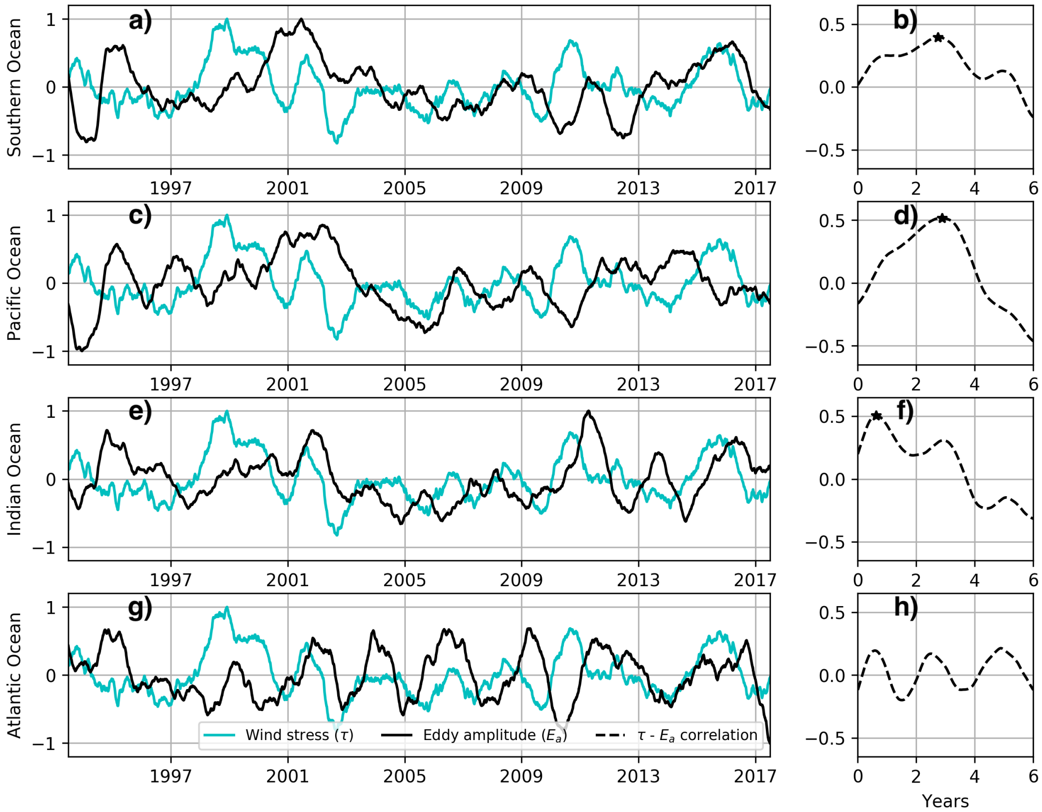

Figure 7. De-trended and normalized time series of the annual running average of eddy mean amplitude (black line) in the Southern Ocean a), Pacific Ocean c), Indian Ocean e) and Atlantic Ocean g) from satellite data and the wind stress anomaly from JRA-55 (cyan line). Dashed lines in plots b, d, f and h corresponds to the cross-correlation between lagged winds and the mean eddy amplitude and the maximum absolute correlation is shown by the stars.

Determining changes to the transient eddy field is fundamental to our understanding of the SO and its potential response to climate change. The Antarctic Circumpolar Current (ACC) comprises of eddies, jets and wave processes. Therefore, understanding the transient variability of the ACC will help us to assess global changes of heat transport and carbon subduction. The presented results indicate that the SO coherent eddy field may be responding to the climate change signal in the wind stress, and motivates us to achieve a better understanding of each process.

There is scope for the proposed method to be refined further in future studies. For example, our decomposition only provides a simple estimate of the Transient Residual Kinetic Energy (TRKE), which could be further separated into the jet and wave flow components. The estimation of TEKE could be improved by further enhancing the optimization fitting code, which currently relies on fixing some eddy properties to constrain the optimization. The assumption of Gaussian eddies may well be violated under strong eddy-eddy, eddy-waves or eddy-jet interactions. We suspect that by introducing additional parameters such as vorticity and/or the phase angle between the meridional v and zonal u components, the identification and reconstruction of eddies could be improved.

In summary, we have developed a new eddy-tracking algorithm with the capability to reconstruct the eddy field and calculate its kinetic energy. We find that the decadal increase in TKE in the SO since the early 1990s is explained by trends in each mesoscale process (coherent eddies and residual). The coherent eddy field has a clear response to the winds intensification and therefore to climate change. This response may have implications on the efficiency of carbon and heat sinks in the Southern Ocean.

Acknowledgments

The satellite altimeter products were produced by Ssalto/Duacs and distributed by AVISO, with support from CNES (https://www.aviso.altimetry.fr/en/data/products/sea-surface-height-products/global/gridded-sea-level-heights-and-derived-variables.html). Murray Fang provided constructive criticism on the first draft of this manuscript. J.M-M. was supported by the Consejo Nacional de Ciencia y Tecnología (CONACYT), Mexico funding. A.K.M. was supported by the Australian Research Council DECRA Fellowship DE170100184. This research was undertaken on the NCI National Facility in Canberra, Australia, which is supported by the Australian Commonwealth Government.

References

Ashkezari, M. D., Hill, C. N., Follett, C. N., Forget, G., & Follows, M. J. (2016). Oceanic eddy detection and lifetime forecast using machine learning methods. *Geophysical Research Letters*, *43*(23), 12234-12241. doi: 10.1002/2016GL071269

Beal, L. M., Ruijter, W. P., Biastoch, A., Zahn, R., Group, S., Cronin, M., ... Zinke, J. (2011). On the role of the Agulhas system in ocean circulation and climate. *Nature*, *472*(7344), 429-436. doi: 10.1038/nature09983

Beron-Vera, F., Olascoaga, M., & Goni, G. (2008, 6). Oceanic mesoscale eddies as revealed by Lagrangian coherent structures. *Geophysical Research Letters*, *35*(12), L12603. doi: 10.1029/2008GL033957

Böning, C., Dispert, A., Visbeck, M., Rintoul, S., & Schwarzkopf, F. (2008). The response of the Antarctic Circumpolar Current to recent climate change. *Nature Geoscience*, *1*(12), 864. doi: 10.1038/ngeo362

Bracegirdle, T. J., Shuckburgh, E., Sallee, J., Wang, Z., Meijers, A. J., Bruneau, N., ... Wilcox, L. J. (2013). Assessment of surface winds over the Atlantic, Indian, and Pacific Ocean sectors of the Southern Ocean in CMIP5 models: historical bias, forcing response, and state dependence. *Journal of Geophysical Research: Atmospheres*, *118*(2), 547-562. doi: 10.1002/jgrd.50153

Chelton, D. B., A, d. R., Schlax, M. G., Naggar, K., & Siwertz, N. (1998). Geographical variability of the first baroclinic Rossby radius of deformation. *Journal of Physical Oceanography*, *28*(3), 433-460. doi: 10.1175/1520-0485(1998)028⟨0433:GVOTFB⟩2.0.CO;2

Chelton, D. B., Gaube, P., Schlax, M. G., Early, J. J., & Samelson, R. M. (2011). The influence of nonlinear mesoscale eddies on near-surface oceanic chlorophyll. *Science*, *334*(6054), 328-32. doi: 10.1126/science.1208897

Chelton, D. B., Schlax, M. G., Freilich, M. H., & Milliff, R. F. (2004). Satellite Measurements Reveal Persistent Small-Scale Features in Ocean Winds. *Science*, *303*(5660), 978-983. doi: 10.1126/science.1091901

Chelton, D. B., Schlax, M. G., Samelson, R. M., & de Szoeke, R. A. (2007). Global observations of large oceanic eddies. *Geophysical Research Letters*, *34*(15), L15606. doi: 10.1029/2007GL030812

Chidichimo, M., Donohue, K. A., Watts, R. D., & Tracey, K. L. (2014). Baroclinic transport time series of the Antarctic Circumpolar Current measured in Drake Passage. *Journal of Physical Oceanography*, *44*(7), 1829-1853. doi:

10.1175/JPO-D-13-071.1

Dong, C., Nencioli, F., Liu, Y., & C, M. J. (2011). An Automated Approach to Detect Oceanic Eddies From Satellite Remotely Sensed Sea Surface Temperature Data. *IEEE Geosci Remote S*, *8*(6), 1055-1059. doi: 10.1109/LGRS.2011.2155029

Dufour, C. O., Griffies, S. M., de Souza, G. F., Frenger, I., Morrison, A. K., Palter, J. B., ... Slater, R. D. (2015). Role of mesoscale eddies in Cross-Frontal transport of heat and biogeochemical tracers in the southern ocean. *J Phys Oceanogr*, *45*(12), 3057-3081. doi: 10.1175/JPO-D-14-0240.1

Faghmous, J. H., Frenger, I., Yao, Y., Warmka, R., Lindell, A., & Kumar, V. (2015, 6). A daily global mesoscale ocean eddy dataset from satellite altimetry. *Scientific Data*, *2*, 150028 EP -. doi: 10.1038/sdata.2015.28

Farneti, R., & Delworth, T. L. (2010). The role of mesoscale eddies in the remote oceanic response to altered southern hemisphere winds. *Journal of Physical Oceanography*, *40*(10), 2348-2354. doi: 10.1175/2010JPO4480.1

Fernandes, A. M. (2009, Aug). Study on the Automatic Recognition of Oceanic Eddies in Satellite Images by Ellipse Center Detection - The Iberian Coast Case. *IEEE Transactions on Geoscience and Remote Sensing*, *47*(8), 2478-2491. doi: 10.1109/TGRS.2009.2014155

Firing, Y. L., Chereskin, T. K., & Mazloff, M. R. (2011). Vertical structure and transport of the Antarctic Circumpolar Current in Drake Passage from direct velocity observations. *Journal of Geophysical Research: Oceans*, *116*(C8), C08015. doi: 10.1029/2011JC006999

Foppert, A., Donohue, K., Watts, D., Tracey, K., Foppert, A., Donohue, K., ... Tracey, K. (2017). Eddy heat flux across the Antarctic Circumpolar Current estimated from sea surface height standard deviation. *Journal of Geophysical Research: Oceans*, *122*(8), 6947-6964. doi: 10.1002/2017JC012837

Frenger, I., Gruber, N., Knutti, R., & Münnich, M. (2013). Imprint of Southern Ocean eddies on winds, clouds and rainfall. *Nature Geoscience*, *6*(8), 608 EP -. doi: 10.1038/ngeo1863

Froyland, G., & Padberg, K. (2009). Almost-invariant sets and invariant manifolds - connecting probabilistic and geometric descriptions of coherent structures in flows. *Physica D: Nonlinear Phenomena*, *238*(16), 1507 - 1523. doi: 10.1016/j.physd.2009.03.002

Froyland, G., Padberg, K., England, M. H., & Treguier, A. (2007). Detection of Coherent Oceanic Structures via Transfer Operators. *Physical Review Letters*, *98*(22), 224503. doi: 10.1103/PhysRevLett.98.224503

Gill, A., Green, J., & Simmons, A. (1974). Energy partition in the large-scale ocean circulation and the production of mid-ocean eddies. *Deep Sea Res Oceanogr Abstr*, *21*(7), 499-528. doi: 10.1016/0011-7471(74)90010-2

Hadjighasem, A., Farazmand, M., Blazevski, D., Froyland, G., Haller, G., Hadjighasem, A., ... Haller, G. (2017). A critical comparison of Lagrangian methods for coherent structure detection. *Chaos: An Interdisciplinary Journal of Nonlinear Science*, *27*(5), 053104. doi: 10.1063/1.4982720

Hallberg, R., & Gnanadesikan, A. (2001). An exploration of the role of transient eddies in determining the transport of a zonally reentrant current. *Journal of Physical Oceanography*, *31*(11), 3312-3330. doi: 10.1175/1520-0485(2001)031⟨3312:AEOTRO⟩2.0.CO;2

Haller, G., Hadjighasem, A., Farazmand, M., & Huhn, F. (2016). Defining coherent vortices objectively from the vorticity. *Journal of Fluid Mechanics*, *795*, 136-173. doi: 10.1017/jfm.2016.151

Hogg, A. M., & Blundell, J. R. (2006). Interdecadal variability of the southern ocean. *Journal of Physical Oceanography*, *36*(8), 1626-1645. doi: 10.1175/JPO2934.1

Hogg, A. M., Meredith, M. P., Chambers, D. P., Abrahamsen, E. P., Hughes, C. W., & Morrison, A. K. (2015). Recent trends in the Southern Ocean eddy field. *Journal of Geophysical Research: Oceans*, *120*(1), 257-267. doi: 10.1002/2014JC010470

Kang, D., & Curchitser, E. N. (2017). On the Evaluation of Seasonal Variability of the Ocean Kinetic Energy. *Geophysical Research Letters*, *47*, 1675-1583. doi: 10.1175/JPO-D-17-0063.1

Klocker, A., & Abernathey, R. (2014). Global Patterns of Mesoscale Eddy Properties and Diffusivities. *Journal of Physical Oceanography*, *44*(3), 1030-1046. doi: 10.1175/JPO-D-13-0159.1

Marshall D., P., Ambaum, M. H., Maddison, J. R., Munday, D. R., & Novak, L. (2017). Eddy saturation and frictional control of the Antarctic Circumpolar Current. *Geophysical Research Letters*, *44*(1), 286-292. doi: 10.1002/2016GL071702

Marshall G., J. (2003). Trends in the Southern Annular Mode from observations and reanalyses. *Journal of Climate*, *16*(24), 4134-4143. doi: 10.1175/1520-0442(2003)016⟨4134:TITSAM⟩2.0.CO;2

Meredith, M. P., & Hogg, A. M. (2006). Circumpolar response of Southern Ocean eddy activity to a change in the Southern Annular Mode. *Geophysical Research Letters*, *33*(16). doi: 10.1029/2006GL026499

Morrow, R., Ward, M. L., Hogg, A. M., & Pasquet, S. (2010). Eddy response to Southern Ocean climate modes. *Journal of Geophysical Research: Oceans*, *115*(C10), C10030. doi: 10.1029/2009JC005894

Nadeau, L.-P., & Straub, D. N. (2012). Influence of wind stress, wind stress curl, and bottom friction on the transport of a model antarctic circumpolar current. *Journal of Physical Oceanography*, *42*(1), 207-222. doi: 10.1175/JPO-D-11-058.1

Nardelli, B. B., Guinehut, S., Verbrugge, N., Cotroneo, Y., Zambianchi, E., & Iudicone, D. (2017). Southern Ocean Mixed-Layer Seasonal and Interannual Variations From Combined Satellite and *In Situ* Data. *Journal of Geophysical Research: Oceans*, *122*(12), 10042-10060. doi: 10.1002/2017JC013314

Nencioli, F., Dong, C., Dickey, T., Washburn, L., & C, M. J. (2010). A Vector Geometry–Based Eddy Detection Algorithm and its Application to a High-Resolution Numerical Model Product and High-Frequency Radar Surface Velocities in the Southern California Bight. *J. Atmos. Oceanic Technol.*, *27*(3), 564-579. doi: 10.1175/2009JTECHO725.1

Patara, L., Böning, C. W., & Biastoch, A. (2016). Variability and trends in Southern Ocean eddy activity in $1/12^o$ ocean model simulations. *Geophysical Research Letters*, *43*(9), 4517-4523. doi: 10.1002/2016GL069026

Richardson, P. (1983). Eddy kinetic energy in the North Atlantic from surface drifters. *Journal of Geophysical Research: Oceans*, *88*(C7), 4355-4367. doi: 10.1029/JC088iC07p04355

Robinson, A. (1983). *Eddies in marine science.* Springer-Verlag.

Souza, J., de Montégut, B. C., & Le Traon, P. (2011). Comparison between three implementations of automatic identification algorithms for the quantification and characterization of mesoscale eddies in the South Atlantic Ocean. *Ocean Science*, *7*(3), 317-334. doi: 10.5194/os-7-317-2011

Tamsitt, V., Drake, H. F., Morrison, A. K., Talley, L. D., Dufour, C. O., Gray, A. R., … Weijer, W. (2017). Spiraling pathways of global deep waters to the surface of the Southern Ocean. *Nature Communications*, *8*(1), 172. doi: 10.1038/s41467-017-00197-0

Tarshish, N., Abernathey, R., Zhang, C., Dufour, C. O., Frenger, I., & Griffies, S. M. (2018). Identifying Lagrangian Coherent Vortices in a Mesoscale Ocean Model. *Ocean Modelling*, *130*, 15 - 28. doi: 10.1016/j.ocemod.2018.07.001

Tsujino, H., Urakawa, S., Nakano, H., Small, J. R., Kim, W. M., Yeager, S. G., … Yamazaki, D. (2018). JRA-55 based surface dataset for driving ocean -

sea-ice models (JRA55-do). *Ocean Model*, *130*, 79 - 139. doi: 10.1016/j.ocemod.2018.07.002

Turiel, A., Jordi, I., & Emilio, G. (2007). Wavelet Filtering to Extract Coherent Vortices from Altimetric Data. *J. Atmos. Oceanic Technol.*, *24*(12), 2103-2119. doi: 10.1175/2007JTECHO434.1

Viikmäe, B., & Torsvik, T. (2013). Quantification and characterization of mesoscale eddies with different automatic identification algorithms. *Journal of Coastal Research*, *65*(2), 2077 - 2082. doi: 10.2112/SI65-351.1

White, M. A., & Heywood, K. J. (1995). Seasonal and interannual changes in the North Atlantic subpolar gyre from Geosat and TOPEX/POSEIDON altimetry. *Journal of Geophysical Research: Oceans*, *100*(C12), 24931-24941. doi: 10.1029/95JC02123

Woloszyn, M., Mazloff, M., & Ito, T. (2011). Testing an eddy-permitting model of the Southern Ocean carbon cycle against observations. *Ocean Model*, *39*(1-2), 170-182. doi: 10.1016/j.ocemod.2010.12.004

Wyrtki, K., Magaard, L., & Hager, J. (1976). Eddy energy in the oceans. *Journal of Geophysical Research*, *81*(15), 2641-2646. doi: 10.1029/JC081i015p02641

Zhang, Z., Wang, W., & Qiu, B. (2014). Oceanic mass transport by mesoscale eddies. *Science*, *345*(6194), 322-324. doi: 10.1126/science.1252418